Fundamental Ice Crystal Accretion Physics Studies

Peter M. Struk, Andy P. Broeren, Jen-Ching Tsao, Mario Vargas, and William B. Wright
Glenn Research Center, Cleveland, Ohio

Tom Currie, Danny Knezevici, and Dan Fuleki
National Research Council Canada, Ottawa, Ontario, Canada

NASA STI Program . . . in Profile

Since its founding, NASA has been dedicated to the advancement of aeronautics and space science. The NASA Scientific and Technical Information (STI) program plays a key part in helping NASA maintain this important role.

The NASA STI Program operates under the auspices of the Agency Chief Information Officer. It collects, organizes, provides for archiving, and disseminates NASA's STI. The NASA STI program provides access to the NASA Aeronautics and Space Database and its public interface, the NASA Technical Reports Server, thus providing one of the largest collections of aeronautical and space science STI in the world. Results are published in both non-NASA channels and by NASA in the NASA STI Report Series, which includes the following report types:

- TECHNICAL PUBLICATION. Reports of completed research or a major significant phase of research that present the results of NASA programs and include extensive data or theoretical analysis. Includes compilations of significant scientific and technical data and information deemed to be of continuing reference value. NASA counterpart of peer-reviewed formal professional papers but has less stringent limitations on manuscript length and extent of graphic presentations.

- TECHNICAL MEMORANDUM. Scientific and technical findings that are preliminary or of specialized interest, e.g., quick release reports, working papers, and bibliographies that contain minimal annotation. Does not contain extensive analysis.

- CONTRACTOR REPORT. Scientific and technical findings by NASA-sponsored contractors and grantees.

- CONFERENCE PUBLICATION. Collected papers from scientific and technical conferences, symposia, seminars, or other meetings sponsored or cosponsored by NASA.

- SPECIAL PUBLICATION. Scientific, technical, or historical information from NASA programs, projects, and missions, often concerned with subjects having substantial public interest.

- TECHNICAL TRANSLATION. English-language translations of foreign scientific and technical material pertinent to NASA's mission.

Specialized services also include creating custom thesauri, building customized databases, organizing and publishing research results.

For more information about the NASA STI program, see the following:

- Access the NASA STI program home page at *http://www.sti.nasa.gov*

- E-mail your question via the Internet to *help@ sti.nasa.gov*

- Fax your question to the NASA STI Help Desk at 443–757–5803

- Telephone the NASA STI Help Desk at 443–757–5802

- Write to:
  NASA Center for AeroSpace Information (CASI)
  7115 Standard Drive
  Hanover, MD 21076–1320

Fundamental Ice Crystal Accretion Physics Studies

Peter M. Struk, Andy P. Broeren, Jen-Ching Tsao, Mario Vargas, and William B. Wright
Glenn Research Center, Cleveland, Ohio

Tom Currie, Danny Knezevici, and Dan Fuleki
National Research Council Canada, Ottawa, Ontario, Canada

National Aeronautics and
Space Administration

Glenn Research Center
Cleveland, Ohio 44135

May 2012

Acknowledgments

Fundamental Ice Crystal Accretion Physics Studies

Peter M. Struk, Andy P. Broeren, Jen-Ching Tsao, Mario Vargas, and William B. Wright
National Aeronautics and Space Administration
Glenn Research Center
Cleveland, Ohio 44135

Tom Currie, Danny Knezevici, and Dan Fuleki
National Research Council Canada
Ottawa, Ontario
Canada K1A 0R6

Abstract

Due to numerous engine power-loss events associated with high-altitude convective weather, ice accretion within an engine due to ice-crystal ingestion is being investigated. The National Aeronautics and Space Administration (NASA) and the National Research Council (NRC) of Canada are starting to examine the physical mechanisms of ice accretion on surfaces exposed to ice-crystal and mixed-phase conditions. In November 2010, two weeks of testing occurred at the NRC Research Altitude Facility utilizing a single wedge-type airfoil designed to facilitate fundamental studies while retaining critical features of a compressor stator blade or guide vane. The airfoil was placed in the NRC cascade wind tunnel for both aerodynamic and icing tests. Aerodynamic testing showed excellent agreement compared with CFD data on the icing pressure surface and allowed calculation of heat transfer coefficients at various airfoil locations. Icing tests were performed at Mach numbers of 0.2 to 0.3, total pressures from 93 to 45 kPa, and total temperatures from 5 to 15 °C. Ice and liquid water contents ranged up to 20 and 3 g/m^3, respectively. The ice appeared well adhered to the surface in the lowest pressure tests (45 kPa) and, in a particular case, showed continuous leading-edge ice growth to a thickness greater than 15 mm in 3 min. Such widespread deposits were not observed in the highest pressure tests, where the accretions were limited to a small area around the leading edge. The suction surface was typically ice-free in the tests at high pressure, but not at low pressure. The icing behavior at high and low pressure appeared to be correlated with the wet-bulb temperature, which was estimated to be above 0 °C in tests at 93 kPa and below 0 °C in tests at lower pressure, the latter enhanced by more evaporative cooling of water. The authors believe that the large ice accretions observed in the low pressure tests would undoubtedly cause the aerodynamic performance of a compressor component such as a stator blade to degrade significantly, and could damage downstream components if shed.

Nomenclature

c	airfoil chord
DAS	Data acquisition system
h	heat transfer coefficient, W/m^{2}K
HD	High-definition
IWC	Ice water content, g/m^3
LWC	Liquid water content, g/m^3
TWC	Total water content, g/m^3
TAT	Total air temperature, °C
ΔT_g	difference between the average surface and recovery temperature

T_{WB} Wet bulb temperature

$T_{WB\infty}$ Wet bulb temperature based on freestream static temperature and pressure

T_{WBo} Wet bulb temperature based on freestream total temperature and pressure

MMD   Median mass diameter, μm

MVD   Median volume diameter, μm

M   Mach number

P_{TOTAL} Total pressure, kPa (absolute)

Re   Reynolds number based on chord

SST   shear-stress-transport (turbulence model)

Subscripts

i   injected

m   measured

Introduction

The aviation industry has experienced numerous engine power loss events associated with high altitude convective weather and often in a warm tropical environment. In 2006, Mason et al. (Ref. 1) suggested that flight in high concentrations of ice crystals has caused ice accretion in core static components of jet engines, especially in the low-pressure compressor region. Such accretions could cause blockages of airflow or even detach and be ingested in further downstream engine components leading to potential surges or stalls. Mason et al. proposed a hypothesis for ice accretion due to ice-crystal ingestion. Essentially, the hypothesis states that ice crystals begin to melt causing mixed-phase conditions within the engine. This mixed-phase water impinges and can accrete on surfaces within the engine even in ambient temperatures above freezing. The accretion continues to grow as long as ice and water continue to impinge until blockage forms where the engine can no longer continue to properly function. The hypothesis specifically states that liquid water is a necessary condition for ice accretion to occur.

In 2007 MacLeod provided additional information on the engine icing phenomena (Ref. 2). In an experiment conducted at facilities of the National Research Council (NRC) of Canada, a heated aluminum plate was placed in ice-crystal conditions and it was demonstrated that rapid ice crystal buildup could be produced on a short time scale. The rapid ice build-up occurred within 30 sec to 2 min depending on the ice crystal concentration. The higher the concentration, the faster the buildup occurred. As the ice shape grew above a critical size, it was ripped off the surface by the velocity of the air moving over the plate. Observations suggested that the ice did not adhere to the surface as in normal super-cooled droplet icing, but was simply held against the stagnation point by the aerodynamic force until some force or moment imbalance resulted in the ice mass being pulled off the face of the block, only to start the cycle over again. As the tunnel velocity increased, the build-up and release cycle became shorter. An alternate explanation may be that the ice had initially adhered to the surface but that the insulating effect of accumulated ice eventually weakens the adhesion because of the internal heating, resulting in ice shed due to aerodynamic force imbalances.

In 2009, Boeing collaborated with NRC and National Aeronautics and Space Administration (NASA) to conduct further ice crystal testing (Refs. 3 and 4) using a rig which simulated the geometry of the S-duct between the low and high pressure compressors in a typical jet engine. The rig included an airfoil which simulated the strut connecting the inner and outer surfaces of this duct. Ice was introduced into a warm airflow and impinged on the test section surfaces, successfully simulating the conditions believed to be present inside the engine core. The tests showed that ice formed on the airfoil and other surfaces of the
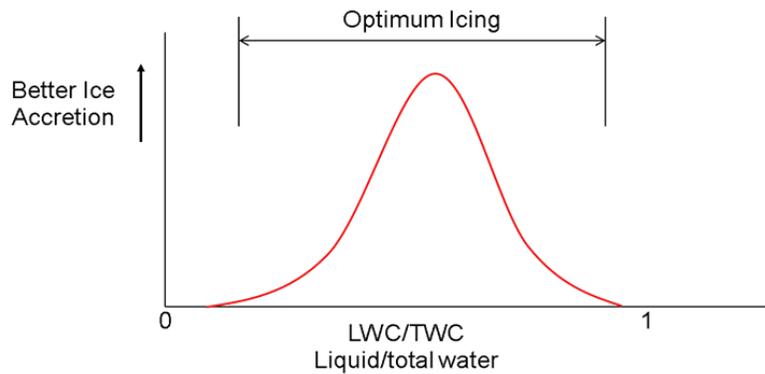
Figure 1.—Conceptual curve showing optimal ice-crystal icing conditions for a given P_{total}, temperature, LWC, TWC (i.e., IWC+LWC), and Mach number.

S-duct at air temperatures significantly warmer than freezing. The authors of this work theorized that an optimum icing regime exists for ice crystal icing which is a function of the ratio of liquid to ice (or total) water content. This region is bounded by conditions where there is not enough ice to cool the surface to the freezing point (i.e., too much liquid) and where there is not enough liquid for the ice to stick and allow heat transfer to take place (i.e., too little water). In between these two boundaries, ice-crystal icing can occur as shown in Figure 1.

NASA and NRC, with sponsorship by the Federal Aviation Administration (FAA) and Transport Canada (TC), are beginning a series of experiments to examine the physical mechanisms of ice accretion on surfaces exposed to ice-crystal and mixed-phase conditions similar to those encountered during engine power-loss events. During November 2010, two weeks of testing occurred at the NRC's Research Altitude Test Facility (RATFac) (Ref. 4). The testing utilized a single wedge-type airfoil placed within a small wind tunnel, called the cascade rig, capable of providing ice-crystal and mixed-phase conditions with altitude (pressure) variation. The objective of the first week of testing was to evaluate the aerodynamic characteristics of the wedge airfoil. The objective of the second week was to begin mapping out the envelope of conditions at which ice accretion occurs in both ice-crystal and mixed-phase conditions. Additionally, these tests included evaluation of a collection of imaging equipment designed to obtain ice accretion measurements of thickness and shape.

A summary of the November 2010 testing is presented in this paper along with some observations and preliminary results. Another set of experiments were conducted at the RATFac during March of 2011 and are discussed briefly in the future work section. Results from those tests are currently being analyzed and will be reported at a later time.

Experiment

Description of Test Facility

The NRC RATFac is outfitted with an ice-crystal generation system and water-spray nozzle system that provide both liquid droplets and ice particles to give the facility the capability to perform testing in ice-crystal and mixed-phase conditions. This facility provides the ability to simulate a wide range of test conditions ranging from a warm engine compressor environment to a cold flight environment for aircraft probe testing. Figure 2 shows how the facility was configured for this testing.
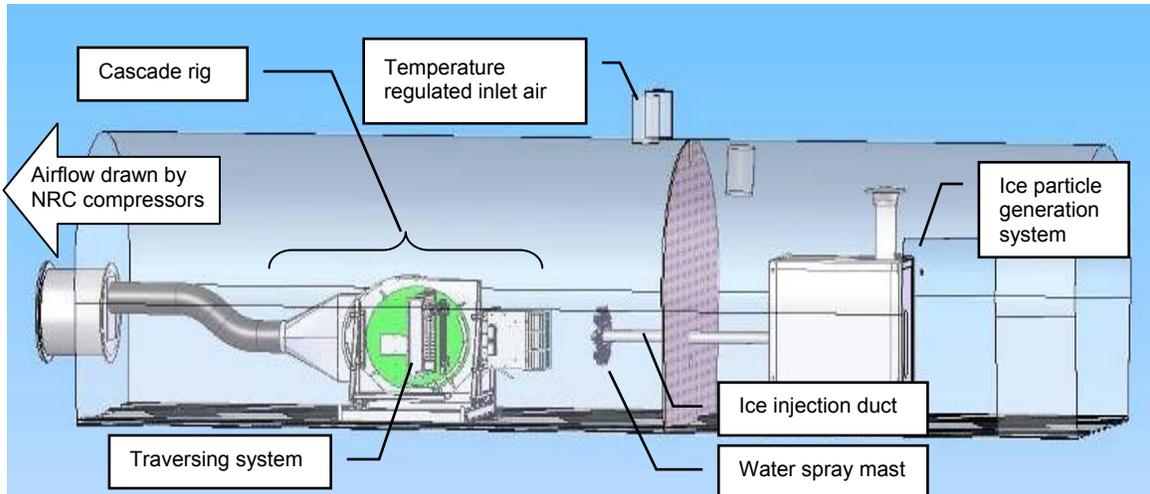
Figure 2.—Ice-crystal test system and cascade wind tunnel installed in the National Research Council of Canada research altitude test facility.

The test cell is divided in two sides by a partition. On the right side of the partition, as oriented in Figure 2, is the cold area where the main part of the ice particle generation system is located. On the left of the partition is the ice-crystals injection duct, the water-spray nozzle system and the cascade-rig wind tunnel. The ice-crystal system controls the mass flow of ice, particle size, and injection of an ice particle laden free jet into the inlet of the cascade rig, Figure 2. A feeder is used to moderate ice flow to obtain the desired ice water content (IWC_i). A grinder generates ice particles with an estimated median mass diameter (MMD) of between 100-300 microns. An injector delivers the ice particles from the grinder to the warm side of the altitude test cell via an injection duct. This system produces an air jet laden with small ice particles that expands to match the inlet to the cascade wind tunnel. The velocity and temperature of the air jet coming out of the injection duct are controlled. Typical operating conditions of the ice-injection jet are exit velocities between 50 to 90 m/sec and temperatures of –15 to –10 °C. The injection duct has a rectangular cross section that measures 50.8 by 177.8 mm.

Natural melting of ice will occur at temperatures above 0 °C and therefore create a mixed-phase condition where liquid and ice phases co-exist. However, to vary LWC independent of other test variables, there is a liquid-water spray mast that can be used to add liquid water to the ice-particle stream. The spray mast, seen in Figure 2, consists of eight nozzles installed as an annulus around the ice-injection duct. The nozzles are installed such that they can be oriented in a wide range of directions to adjust the spray plume to suit the wind-tunnel inlet or test article geometry. The nozzles are air-assist atomization nozzles which can produce a MVD between 20 and 40 microns over the LWC range (up to ~3 g/m^3). Although mixed-phase testing is typically conducted above 0 °C, the water and atomization air are heated to mitigate droplet freeze out. In order to permit a large range of LWC's at a fixed MVD, the number of nozzles injecting water can be varied from 8, 4, or 2. A more detailed discussion of this system can be found in Reference 4.

Cascade Wind Tunnel

These experiments were performed using the NRC cascade wind tunnel (Figure 3). The wind tunnel consists of an inlet duct with a bell mouth rectangular inlet and test section. The dimensions of the test section at the location where the airfoil was mounted are 132 by 254 mm. The ice-laden air jet, liquid-water spray plume, and temperature-regulated air entering the altitude chamber are drawn into the inlet bell mouth. These flows mix together and travel approximately 1.27 meters along the inlet duct before reaching the test article. The inlet duct can be fully characterized upstream of the test article using a
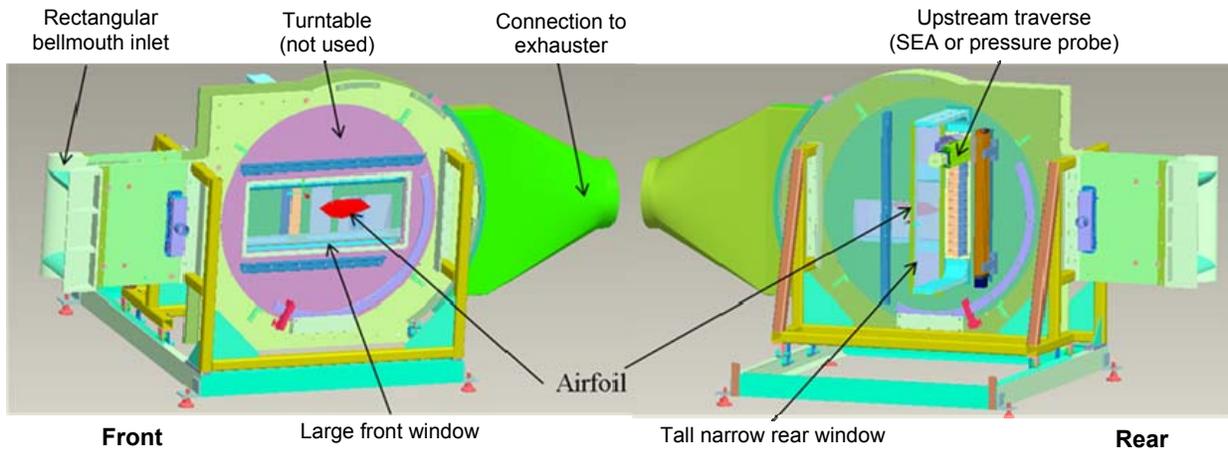
Figure 3.—Cascade wind tunnel showing experimental configuration including airfoil.

TABLE 1.—GENERAL OPERATING RANGE OF THE ICE-
CRYSTAL TESTING CAPABILITIES FOR THE CASCADE
WIND TUNNEL IN THE NATIONAL RESEARCH COUNCIL
OF CANADA'S RESEARCH ALTITUDE TEST FACILITY

Parameter	Unit
$-40 < TAT^a < +35$	°C
$\sim150 < alt. < \sim12{,}000$	meters
$0.15 < M < 0.8$	
$2 < IWC_i < 10$	bulk, g/m^3
$100 < MVD_{ice} < 300$	μm
$0.5 < LWC < 4$	g/m^3
$20 < MVD_{water} < 40$	μm

[a]Total air temperature.

traversing system. For mixed phase testing, a multi-element hot-wire probe developed by Science Engineering Associates is typically used on the traversing system to measure LWC and TWC. The general operating range of this test system is outlined in Table 1 with the detailed operating characteristics of the facility provided in Reference 5.

Setting Operating Point

Test points are attained by initially setting the Mach number, altitude, and total temperature. The total pressure and total temperature are measured by a fixed probe attached to the top end wall. A static tap on the upper end wall was used to determine the static pressure to calculate Mach number and static conditions. These test parameters were set under dry conditions, i.e., before the ice and/or water flow was started. Given the inaccuracy of hot wire probes when measuring solid or melted ice particles (Ref. 4), the ice-water content of the flow can be set in two ways. Firstly, this can be established based on bulk calculations where the mass flow of ice is set given the volume flow of air to achieve a desired ratio of ice mass to dry-air volume (e.g., g/m^3)—this is referred to as injected ice-water content (IWC_i). The liquid-water content is measured (LWC_m) at the centerline typically using the TWC scoop element of the multi-element probe before the test point is run. This water-flow setting is then noted and utilized to provide the desired supplemental LWC. In this paper, values measured by the multi-element probe are referred to with the subscript "m" (e.g., TWC_m and LWC_m) to differentiate them from the injected values (e.g., IWC_i and LWC_i). The measurement accuracies of these test parameters are outlined in Table 2.

TABLE 2.—MEASUREMENT ACCURACY
OF TEST SYSTEM PARAMETERS

Parameter	Accuracy
TAT	±0.5 °C
Total pressure	±0.14 kPa
Mach number	±0.004
Liquid-water content	±10%
Angle of attack	±0.5°

Test Article (Airfoil) Design and Instrumentation

Requirements

Since the purpose of the tests was to study the fundamental physics of ice-crystal icing, the geometry of the test article was selected to facilitate this while still retaining critical features of a compressor stator blade or guide vane. In particular, a sharper leading edge is used than would typically be found on an isolated airfoil designed for subsonic freestream Mach numbers. The blade shape was also selected to permit ice particles to impact its pressure surface at high (closer to normal) incidence angles, for the following reason. Assuming ice particles entering the rotor are large enough to travel more or less ballistically (i.e., follow the flow poorly), a significant percentage will likely impact the rotor blade pressure surfaces due to mismatched blade and particle tangential velocities. The velocities of these particles relative to the rotor will be reduced by friction with the blade surfaces, resulting in reduced axial and increased tangential velocity components in the absolute reference frame on exit from the rotor. The resulting trajectory will cause the particles to impact the pressure surface of a downstream stator at higher incidence than the airflow.

Specific requirements that guided the selection and design of the test article were as follows:

(1) The test surface was required to have significant areas of low tangential velocity, with high particle incidence angles, to maximize the likelihood of ice adhering.
(2) Good optical and mechanical access to the test surface was required to facilitate measuring and observing the ice accretion process.
(3) A predominantly flat impingement surface with uniform wall thickness was required to facilitate mounting instrumentation, thin film heaters, etc., and facilitate setting optimum viewing angles for imaging and other optical techniques. Calculation of particle impingement angles would also be simplified with a flat surface, particularly for particles large enough to have ballistic trajectories.
(4) Easy access to the back side of the test surface was required to facilitate attachment of heating and cooling equipment, thermocouples, and other transducers.
(5) The (ice-free) test geometry was required to be free of large regions of separated flow which could modify the flowfield around the icing surface.

Geometry

Based on the above requirements, the symmetrical wedge airfoil shown in Figure 4 was selected as the test article. This airfoil consists of a 40° (total included angle) wedge forebody and a 20° (total included angle) linearly tapered afterbody, connected by 86.61 mm radius 30° circular arcs. The leading edge is a 2:1 ellipse with a thickness of 3.76 mm where it transitions to the 50.8 mm straight lines on the forebody, while the trailing edge is a 1.0 mm radius circular arc. The airfoil span is 132.1 mm, its chord is 220.93 mm, and the maximum thickness is 48.97 mm, giving a thickness-to-chord ratio of 0.222. Points defining the geometry are included in the Appendix.
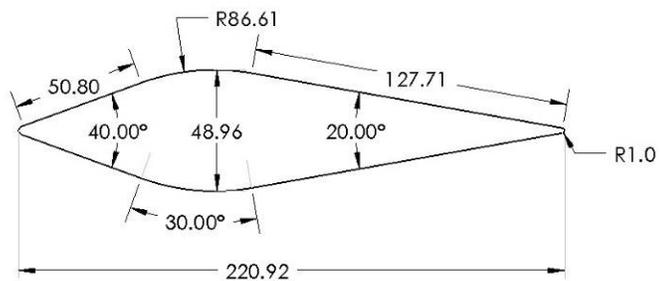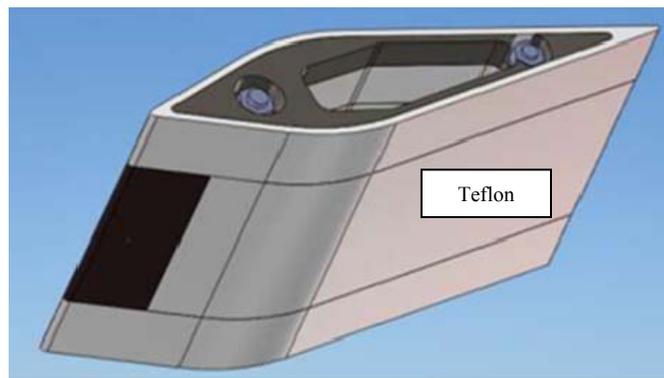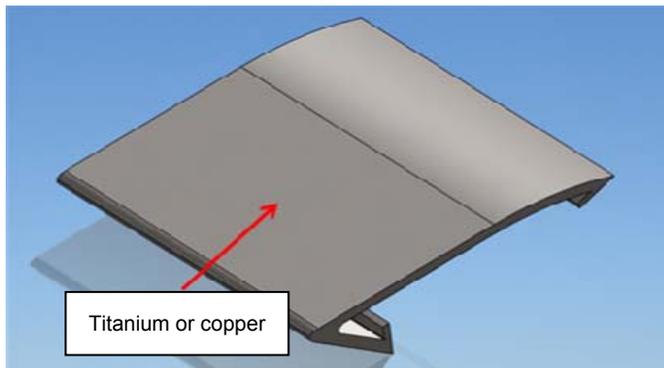
Figure 4.—Images and drawings of the airfoil including image of airfoil mounted in the test section (top), surface used in icing airfoil (upper middle), lower side of icing airfoil (lower middle), and airfoil cross-section with dimensions in mm (bottom). The airfoil is mounted at a –6° angle of attack with the leading edge canted downward relative to oncoming air as seen in the top image.

The aerodynamic design of the test article was performed iteratively with the CFD code ANSYS CFX (version 12.1), which predicted the final geometry would be largely stall-free for angles of attack up to 10° in the icing tunnel, for the desired range of test conditions, which included Mach numbers from 0.2 to 0.4, total pressures (absolute) from 45 to 93 kPa, and total temperatures of 0 to 15.6 °C. The corresponding chord Reynolds number range is ~0.45×10^6 to 1.8×10^6. The critical Mach number at 0° angle-of-attack is approximately 0.50. For the November 2010 tests, the airfoil was set at a –6° angle of attack (i.e., the leading edge of the airfoil was canted downward relative to the oncoming flow). At –6° angle-of-attack, the critical Mach number is calculated to be approximately 0.46.

Test Surface Design & Instrumentation, Icing, and Heat Transfer Tests

The test surface was the pressure surface segment of a copper (C11000) or titanium (Ti 6Al-4V) insert in an otherwise Teflon (DuPont, Wilmington, DE) airfoil, as seen in Figure 4. The copper insert was used for single-phase (air) convective heat-transfer tests, while the titanium insert was used for icing tests. This alloy of titanium is representative of the material used to make jet-engine compressor components. Teflon was chosen for the rest of the airfoil because of its low thermal conductivity and its expected resistance to ice adhesion so as to minimize the ice accretion near the windows and in the areas not covered by the titanium alloy plate.

The spanwise dimension of the insert was set to 76.2 mm to keep it out of the endwall boundary layers, which were estimated to be approximately 25 mm thick at the location of the airfoil. The pressure surface segment of the insert included the 50.8 mm flat section of the wedge forebody plus 23.6° of the 86.61 mm radius 30° circular arc, while the suction surface segment was truncated at 29.4 mm from the start of the flat section to allow better access to the back side of the pressure surface. The wall thickness of the insert was nominally 3.175 mm (coordinates are included in the Appendix). An air gap of 1.5 mm was maintained between the insert and the Teflon, so the back side of the insert wall was effectively thermally insulated, producing a wall thermal boundary condition similar to a hollow compressor blade. Six 12.7 by 50.8 mm thin film Kapton heaters (OMEGA KHLV-0502-10-P, DuPont, Wilmington, DE) were attached to the back surface of the insert wall to create a surface heat flux for convective heat transfer coefficient measurements, and deicing.

The heat flux through the surface of the copper insert was measured at four locations with RdF 27134-2 thin-film heat-flux gauges, as shown in Figure 5. These gauges, which measure 7.87 by 12.7 by 0.165 mm thick, were installed in pockets cut to the size and thickness of the gauges so they would be flush with the surface. The gauge centroids were located at chordwise (x) locations of 8.13, 20.07, 32.0, and 43.94 mm, and spanwise distances of +16, –16, +6.48, and –6.48 mm, measured from center span towards the tip. The gauges were staggered on either side of center span to prevent the wakes of the heat flux gauge and thermocouple wires from interfering with the heat fluxes measured by the gauges downstream.
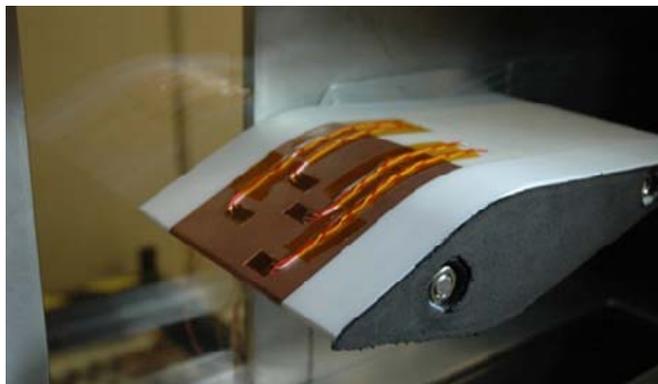

Figure 5.—Airfoil with copper insert used to measure the surface heat transfer coefficient.

TABLE 3.—INSERT THERMOCOUPLE
LOCATIONS

| Thermocouple	x (mm)	y (mm)
1	1.40	0.0
2	38.56	14.22
3	24.94	9.27
4	52.17	19.15
5	66.37	22.50
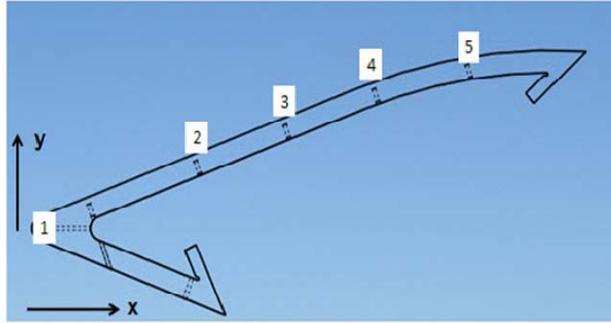
Figure 6.—Cross-section of airfoil insert showing
thermocouple locations.

Both the copper and titanium inserts were fitted with five calibrated 36 gauge type K thermocouples
at the nominal (bead) locations indicated in Table 3 and shown in Figure 6. These thermocouples were
epoxied into 0.8 mm diameter holes drilled to a distance of 0.75 mm from the outer surface, at mid span.

Aerodynamic Tests

The 76.2 mm span center section of the wedge airfoil into which the titanium and copper test surfaces
were inserted was replaced with a hollow aluminum section for the aerodynamic tests as shown in
Figure 7. The aluminum center body contained forty-two 0.5 mm diameter static taps at mid span for the
purpose of measuring the static pressure distribution, and thereby determining the isentropic Mach
number distribution, around the airfoil profile. The measurements were performed using an electronically
scanned pressure system referenced to the test section static pressure.

Surface-oil flow visualization was also performed for a limited number of conditions to verify the
flow uniformity. The aluminum surface of the model was covered with a white, self-adhesive plastic film.
This provided a smooth surface for the oil to flow and good color contrast. The oil-flow mixture consisted
of Demco #702 lamp black pigment in Rexall (Heavy) Mineral Oil. It was applied to the model surface
using a sponge roller commonly used in trim painting applications. Photographs were taken before and
after each run along with real-time video. The video display was monitored during the run to ensure
that steady-state conditions were achieved in the surface-oil flow. After each run, it was possible to
re-distribute the oil-flow mixture on the surface using the sponge roller, thus eliminating the need to
clean and re-apply the oil coating.
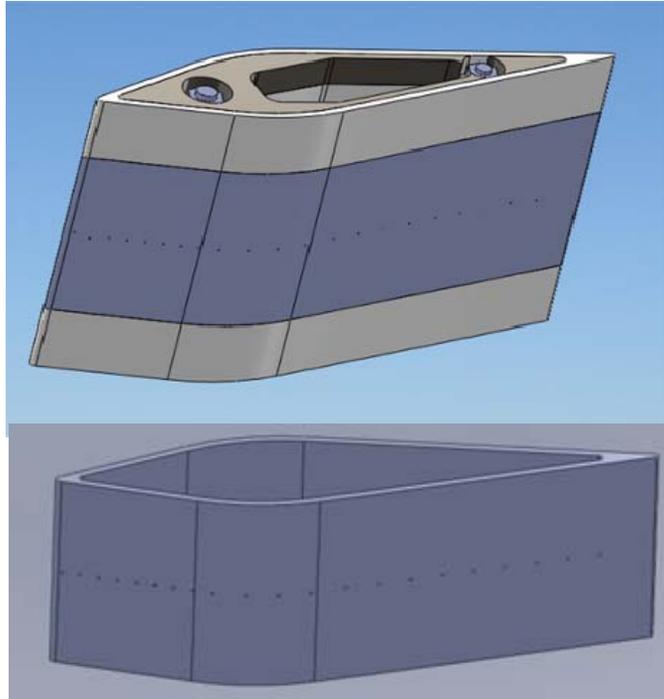
Figure 7.—Airfoil (top) with aluminum center body (bottom) showing static taps along mid section.
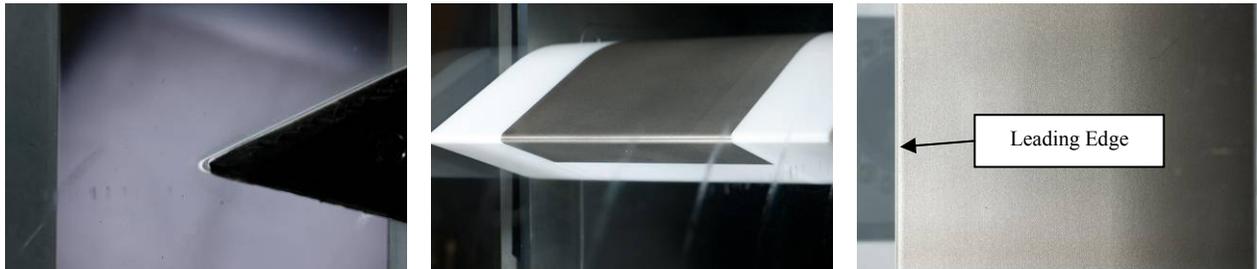
Figure 8.—The 3 views imaged during testing prior to ice: a side backlit view (left), a front perspective view (center), and a top down view (right). In the right-most image, the flow direction is from left to right.

Video Imaging Diagnostics

Still image and video cameras captured high resolution image data during each test run. Figure 8 shows three primary views captured with the still cameras. The test section had clear acrylic windows on both sides allowing for a backlit image to be captured (Figure 8, left). The backlit view was intended to capture ice-shape profiles as they develop on the airfoil. A front perspective (Figure 8, center) was also imaged allowing a view of both the top (pressure) and bottom (suction) surface of the airfoil. Additionally, the test section had a long narrow window along the top wall, allowing a camera to image the airfoil normal to the icing surface, denoted as the top-down view (Figure 8, right). A high-definition (HD) video camera imaged a view similar to the top-down view on a slightly parallel axis to allow real time feedback of the icing in the control room. Finally, a high-speed camera was used to capture some surface phenomenon such as particle impingement, splashing, and shedding during select tests. Images from the high-speed camera have yet to be analyzed and are not presented in this paper.

The still cameras (Nikon model D3X) captured images at a resolution of 6048 by 4032 pixels at a frequency of 1 every 5 seconds (although up to 1 per second was possible). The number of images

captured was pre-programmed and was typically 60, spanning 300 seconds. The cameras were manually triggered at the beginning of a test (usually just prior to initiating the ice and/or water spray) and ran continuously for the pre-programmed number. Occasionally, a second round of images was triggered depending on whether the test duration was increased or was not known prior to test initiation. Synchronization between the 3 still cameras was achieved by opening the shutters on the camera and firing a bright flash at a very short duration. The HD camera (Sony FCB-H11) produced images at resolution of 1280 by 720 pixels at a rate of 60 frames per second. The flash from the still camera system saturated the HD camera image for a frame or two, thereby leaving a marker in the video data which allowed later synchronization with the still cameras.

The imaging data were intended for both observations and quantitative measurements. The top-down view allowed measurement of the ice accretion growth against time. The side backlit view allowed measurement the ice-shape profile during the ice-accretion event although no ice profiles will be presented at this time. The three views combined also allowed for tracking the chordwise ice-accretion formation limits during the ice accretion event.

Results

Aerodynamic Tests

The purpose of these experiments was to characterize the airfoil surface-pressure distribution and surface flowfield. Two angles of attack, 0° and –6° were investigated at Mach 0.2, 0.3 and 0.4, and nominal stagnation pressures of 45 and 93 kPa. This represents a chord Reynolds number range from approximately 0.45×10^6 to 1.8×10^6 corresponding to the lowest pressure and Mach number to the highest pressure and Mach number, respectively. The total air temperature ranged from approximately 8 to 20 °C for these tests. Surface-pressure measurements were performed with and without the ice-injection air flowing (sans ice crystals) to confirm that there was no effect of the injection-air jet on the pressure distribution. Several repeat runs were also performed demonstrating good repeatability in the data.

The baseline pressure data for 0° angle of attack are shown in Figure 9. Three sets of data are plotted. The uncorrected experimental data were plotted as measured on the airfoil. These data were corrected
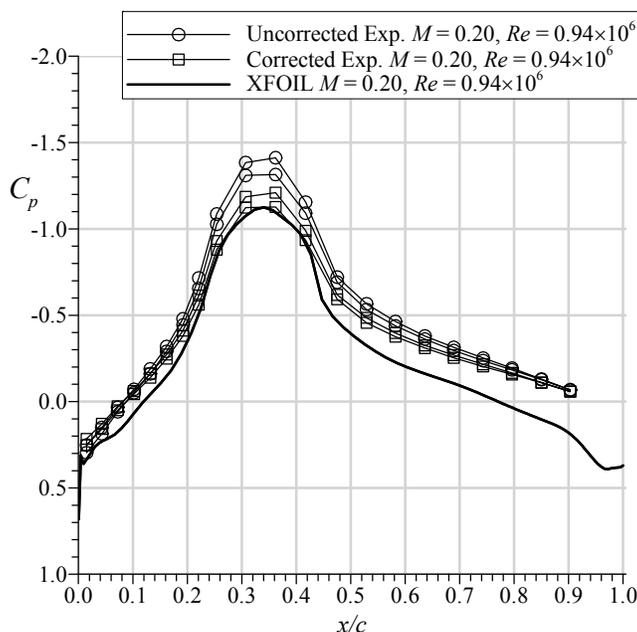

Figure 9.—Comparison of airfoil surface pressure data at
α = 0 and p_o = 93 kPa.

using the methods of Barlow et al. (Ref. 6) and Allen and Vincenti (Ref. 7). This correction amounted to an increase in the dynamic pressure accounting for estimated solid- and wake-blockage effects. The methods were intended for two-dimensional testing with model chord-to-tunnel height ratios much less than those used here. Since the main purpose of this research was focused on ice-accretion physics and not aerodynamics, the relatively large size of the model was not an over-riding concern. The pressure distribution was analyzed using XFOIL (Ref. 8) at matched Reynolds and Mach number. The XFOIL drag coefficient was used in the formulation for the wake blockage portion of the wake-blockage correction. The experimental pressure distributions indicate that there was a small asymmetry, most likely in the airfoil angle of attack. This minor asymmetry was considered negligible since the ice accretion testing was performed at –6° angle of attack. The corrected experimental data matches the XFOIL results fairly well from the leading edge to about $x/c = 0.42$. It is likely that the disagreement in surface pressure was due to uncorrected blockage effects. The elevated suction pressures in the experimental data relative to the XFOIL results indicated higher local velocities symptomatic of larger blockage. Despite these effects, the pressure data at 0° angle of attack provided confidence in the experimental methods and measurements.

All of the ice accretion testing was performed with the airfoil at an angle of attack of –6°, for which a pressure distribution comparison is shown in Figure 10. Here the uncorrected experimental data are plotted with results from a three-dimensional CFD analysis computed using ANSYS CFX (version 12.1). The simulation models a half span of the test section from the bell mouth inlet to 3.5 axial chord lengths downstream of the airfoil. A plane of symmetry defines the boundary condition at mid span. The steady-state RANS simulation employs the shear-stress-transport (SST) turbulence model. A second-order central differencing scheme performs the discretization of the governing equations. The endwall, upper- and lower-control surface, and airfoil boundary layers are assumed to be fully turbulent. The structured hexahedral mesh was determined to be grid independent with 1.3 million nodes.

In Figure 10, agreement on the forward portion of the airfoil between the experiment and CFD results is good and indicates a slight mismatch in angle of attack (or lift coefficient). It should also be noted that the suction-surface pressure coefficients at $x/c = 0.36$ and 0.42 were not available due to installation anomalies. Better matching with the suction-surface pressure recovery region may have been shown were these pressure coefficients measured. Most importantly, there is excellent agreement between the experimental and CFD data on the pressure surface upstream of $x/c = 0.25$ which was the icing-test surface of interest. Surface-oil flow visualization was also performed for these conditions. Flow on the pressure surface of the airfoil was two dimensional and separation free. On the suction surface there was evidence of a small separation bubble on the leading edge associated with the steep adverse pressure gradient and small leading-edge radius. This small, stable bubble did not negatively impact the flow on the pressure surface of interest for the icing studies. The same is true of boundary-layer separation near the trailing-edge on the suction surface.

The effects of Mach number and Reynolds number variation for the –6° angle of attack configuration are shown in Figure 11. Classic compressibility effects were observed in the increasing suction pressure centered near $x/c = 0.36$ on the pressure surface. This was not as clear on the suction surface. This may not have been observed because of the unavailable pressure data at $x/c = 0.36$ and 0.42. In addition, the behavior of the suction surface pressures were influenced by the trailing-edge separation noted in the surface-oil flow visualization. Taken as a whole, the surface pressure and flow visualization information confirm that the flow over the icing surface on the pressure side was well-behaved for the ice-accretion studies over the desired range of conditions.
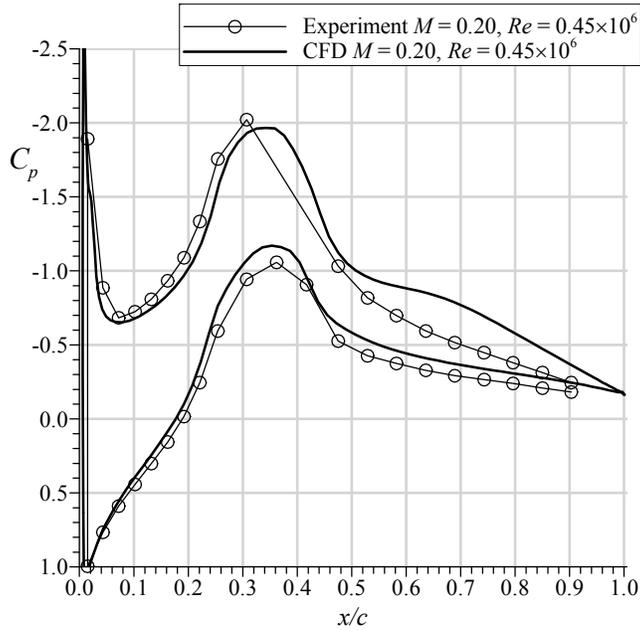
Figure 10.—Comparison of airfoil surface pressure data at $\alpha = -6°$ and $p_o = 45$ kPa.
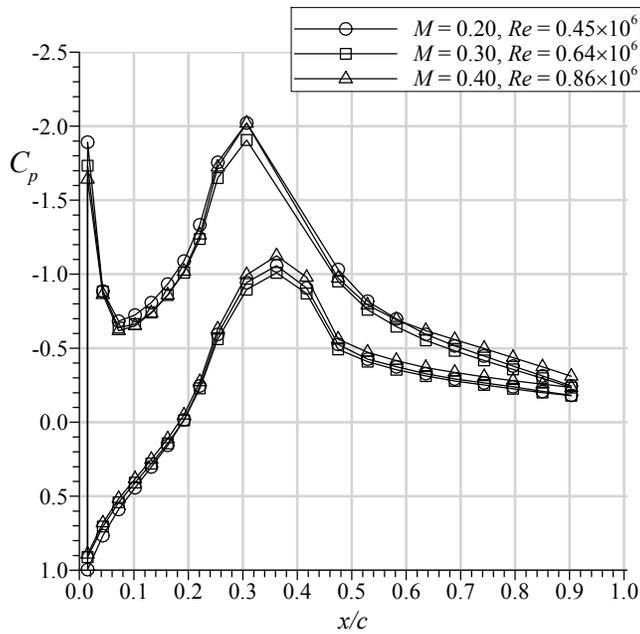
Figure 11.—Effect of Mach and Reynolds number on measured airfoil surface pressure distribution at $\alpha = -6°$ and $p_o = 45$ kPa.

Heat Transfer Tests

The copper insert with the flush-mounted heat-flux gauges was used to measure heat-transfer coefficients at tunnel Mach numbers of 0.215, 0.25, and 0.32; and a total temperature and total pressure of ~10 °C and 45 kPa, respectively. The total temperature was measured with a traversing probe approximately 15.2 cm upstream of the airfoil leading edge, directly in front of the wedge airfoil pressure surface.

The total temperature of 10 °C was achieved by mixing cold air at ~ –15 °C from the ice injection duct with warm air from the altitude chamber, as done in the icing tests. The velocity of the cold air jet at exit from the ice injection duct was fixed at ~84 to 85m/s , which differed somewhat from the values used in the icing tests, which were typically 50 to 62 m/s and 71 to 72 m/s at M = 0.2 and 0.3, respectively.

The total power supplied to the five identical thin film heaters attached to the back side of the copper insert was fixed at 55.7 W for all tests, which was sufficient to produce a difference between the average pressure-surface copper temperature and the recovery temperature, designated ΔT_{sa} , of ~32.1 °C at M = 0.215 and ~26.7 °C at M = 0.322. The spread in the temperatures of thermocouples 2 to 5 in Figure 6 was within 6% of ΔT_{sa} in all tests, although the temperature of thermocouple 1 (leading edge) was 15 to 17% of ΔT_{sa} below the average pressure-surface copper temperature. These differences will be ignored, and the heat transfer coefficients calculated from the measured heat fluxes and ΔT_{sa} will be assumed to apply to an isothermal surface.

The heat fluxes obtained from the gauges were first converted to a heat-transfer coefficient using the difference between the recovery temperature, calculated assuming a laminar boundary layer recovery factor of 0.84, and the estimated surface temperature of the heat flux gauge. The latter was calculated by multiplying the gauge heat flux by its thermal impedance, calculated from the gauge geometric parameters and material conductivities, and subtracting the resulting gauge temperature difference (ΔT_g) from the measured temperature of the copper underneath the gauge. The difference ΔT_g was 16 to 18% of ΔT_{sa} for the gauge nearest the leading edge, and 11 to 13% for the gauges downstream. The depressed gauge surface temperatures would have caused the measured heat fluxes to be lower than they would have been if the gauge surface temperature had been equal to the copper temperature, so steady-state RANS CFD simulations with ANSYS CFX were performed to correct for this effect. This was done for each test condition by first simulating flow over the wedge airfoil with the measured pressure surface average temperature, $T_{PS,AVE}$, applied to the surface of the copper, and temperatures applied to the gauge surfaces which matched their estimated temperatures in the experiments (i.e., $T_{PS,AVE}$ - ΔT_g). These simulations were performed with the SST turbulence model and gamma-theta transition model, with the turbulent intensity upstream of the airfoil (at the probe traverse plane) set to the value measured by Knezevici and Fuleki (Ref. 5). A turbulence model was used because preliminary calculations for laminar flow indicated that the measured heat transfer coefficients were typically 60% higher than laminar values. Matching the turbulent length scale to the measured value (Ref. 5) produced heat transfer coefficients typically 25% above the measured values, so the length scale was adjusted until the predicted heat transfer coefficients over the gauges with the depressed gauge surface temperatures matched the corresponding measured values within 5%. This typically required a fourfold reduction in the length scale from the measured value. The simulation was then repeated with the surface temperatures of the gauges set to the temperature of the copper, resulting in a new set of values for the heat transfer coefficients over the gauges. The ratio of the new (isothermal surface) heat transfer coefficients to the values predicted with the depressed gauge surface temperatures were then multiplied by the measured heat transfer coefficient, calculated as described previously using the estimated gauge surface temperature, to correct the measured value. The corrections were small for the heat flux gauge nearest the leading edge, less than 3%, but increased the measured heat transfer coefficients for the downstream gauges, calculated with the depressed gauge surface temperatures, by 21 to 29%. The resulting corrected heat transfer coefficients (h) are given in Table 4. The estimated uncertainty in the corrected values is ±15%. Values are not available for the gauge at x = 20.0 mm because it malfunctioned in the tests.

TABLE 4.—MEASURED HEAT TRANSFER
COEFFICIENTS (W/M^{2}K)

M	h x = 8.13 mm	h x = 32.0 mm	h x = 43.94 mm
0.215	160.4	111.9	120.2
0.25	166.0	137.2	135.7
0.32	180.0	161.1	142.6

Icing Tests

During the second week of testing in November 2011, icing tests were performed for flow speeds ranging from M = 0.2 to 0.3 at P_{TOTAL} from 93 to 45 kPa and TAT from 5 to 15 °C. Ice- and liquid-water contents ranged up to values of 20 and 3 g/m^3, respectively. The test matrix followed is shown in Table 5. The matrix only shows runs with ice or water injection as these correspond to when image data were taken. The run numbers follow a sequential order and correspond to the computer filename assigned by the facility data acquisition system for that given run. Numbers missing in the sequence generally represent calibrations or readings of steady-state conditions just prior to initiating an icing run.

Table 5 shows the key parameters controlled for a particular run including TAT, M, P_{TOTAL}, IWC_i, LWC_i, as well as the targeted duration of the run labeled "Time." As the run duration is a manually controlled process, the actual run durations varied somewhat and in some cases continued beyond the target duration to allow the icing to continue or to make measurements of TWC_m and LWC_m by inserting the multi-wire probe. In general, conditions were kept steady during the run. However, a limited number of runs varied the IWC or LWC in discrete increments during a single run which were labeled as "sweeps." The sweeps were intended to find a threshold value where ice accretion would initiate. Additionally, runs were conducted during which the multi-wire probe made measurements at different discrete locations along the tunnel. These runs were called a traverse but are not reported here.

During analysis of the test results, a wet-bulb temperature appeared to be useful to describe when icing would and would not occur. The temperature of a wet adiabatic surface in airflow is the wet-bulb temperature (T_{WB}), which is a function of the air dry-bulb temperature, pressure, and moisture content. T_{WB} is obtained by equating the rate of heat transfer to a surface by convection to the heat loss by evaporation, assuming any water added to replace that lost by evaporation, and therefore keep the surface wet, is at T_{WB}. As such, wet-bulb temperatures based on freestream static and total temperature and pressure, designated $T_{WB\infty}$ and T_{WBo}, respectively, were calculated post-test and are included in Table. 5. The moisture content used to calculate $T_{WB\infty}$ and T_{WBo} was not measured in the cascade tunnel with a hygrometer, but rather was determined from a mass balance on moisture entering the tunnel via the cold injection air (dew point ~ –50 °C) and air entering the tunnel from the altitude chamber, which had the same moisture content as outside ambient. The latter was measured at the inlet for outside air with a dew point sensor. The two wet-bulb temperatures were not adjusted to account for evaporation of liquid water produced by the melting of ice or injected with the spray system.

TABLE 5.—ICING TEST MATRIX PERFORMED DURING THE NOVEMBER 2010 PROGRAM

Run	Objective	M	P_{TOTAL} kPa	TAT °C	T_{WBo} °C	$T_{WB\infty}$ °C	Time min.	IWC_i g/m³	LWC_i g/m³	TWC_m g/m³	LWC_m g/m³	Results
97	IWC & *LWC* injection	0.20	93	14.6	5.7	4.4	3	8	2	N/A	N/A	No ice accretion.
98	IWC injection only	0.20	93	14.6	5.7	4.4	3	8	0	2.8	0.9	No ice accretion.
101	IWC sweep	0.20	93	11.9	5.2	3.9	17	4-12	0	N/A	N/A	Slushy ice accretion started at 7 g/m³ with small clumps of ice building and shedding repeatedly. No significant accumulations.
103	IWC sweep	0.20	93	5.8	1.8	0.4	11	5-14	0	N/A	N/A	Small ice accretion started at ~7 g/m³. However, there was a rather substantial ice growth by run end and no shedding.
115	IWC injection only	0.21	93	5.6	Super sat	Super sat	3	9	0	3.9	1.2	Only trace of irregular ice accretion with small shed events.
117	IWC injection only	0.21	93	5.3	5.0	Super sat	3	14	0	6.5	1.5	More uniform accumulation with leading edge ice growth and shed.
121	IWC injection only	0.20	93	6.2	3.7	2.3	3	20	0	8.7	1.7	Uniform ice accretion with leading edge growth which may have reached a steady state thickness. No shedding observed.
126	IWC sweep	0.30	93	15.2	5.6	2.6	15	2-14	0	N/A	N/A	Ice accretion began at 2 g/m³ and increased with higher IWC. Ice looks more solid than M = 0.2 cases with smaller overall shape.
132	*LWC* sweep	0.30	93	6.8	1.3	−1.5	6	10	0,0.5,1	6.5	1.5	No accretion without LWC. As LWC added, ice accretes near leading edge and on suction surface. Ice appears uniform.
135	*LWC* sweep (high to low)	0.29	93	7.6	1.8	−1.7	8	10	3,2,1	N/A	N/A	No ice accretes initially with high LWC. As LWC reduced, a trace amount of slushy ice accretes near the leading edge.
137	*LWC* injection: 2 nozzles	0.20	45	11.3	−3.1	−4	2.6	0	1	1.3	1.0	Glaze ice forms across entire airfoil including suction surface.
139	*LWC* injection: 4 nozzles	0.20	45	12.5	−2.7	−3.7	6.7	0	1	1.1	0.9	Large glaze ice formation across entire airfoil including suction surface.
141	IWC injection only	0.20	45	13.8	−2.1	−3	3	5	0	1.5	0.2	Very small ice accretion just near leading edge. Possibly thin ice layer on the forebody pressure surface
144	IWC & *LWC* injection	0.20	45	14.6	−1.8	−2.5	4.5	5	1	3.4	1.3	Large ice accretion to about half way up flat portion of airfoil. Continuous leading edge ice growth.
147	IWC injection only	0.21	45	12.3	−3.6	−4.6	3	5	0	1.58	0.16	Very thin layer of ice formed across entire forebody pressure surface. Layer disappears quickly after ice off.
149	IWC & *LWC* injection	0.21	45	11.9	−3.7	−4.7	3	5	2	5.2	2.2	Very large ice accretion to about 3/4 of the way up flat portion of airfoil. Rapid continuous leading edge ice growth.
151	Ice erosion run	0.21	45	13.4	−3.1	−4.2	5+1.5	5	2	5.9	2.2	Built up ice formation with LWC for 5 minutes then added IWC for 1.5 min. Rather than erode, ice continually grew & shed.
155	IWC injection only	0.30	45	12.9	−3.3	−5.4	3	5	0	1.7	0.17	No accretion.
158	IWC & *LWC* injection	0.30	56	14.8	−0.3	−2.5	3.5	5	1.5	5.2	1.7	Ice accretion near leading edge with measureable thickness ahead of leading edge. Aft impingement limit close to leading edge.

The testing began at a low-altitude pressure of 93 kPa and represented conditions similar to those used in earlier testing (Refs. 3 and 4). For runs with higher TAT values and IWC values of 8 g/m^3, no ice accumulation was observed on the airfoil both with and without LWC (runs 97-98). For larger IWC$_i$ values during the sweeps, only trace amounts of ice were observed for the warmer TAT condition (run 101) but significantly more accumulation was observed at the colder TAT condition (run 103) especially with larger IWC$_i$ values in the sweep.

Runs were thus continued at lower TAT conditions at 93 kPa. With an IWC of 9 g/m^3, run 115 produced a thin layer of slushy ice in an irregular pattern near the stagnation region of the airfoil. For run 117, an IWC$_i$ 14 g/m^3 was large enough to yield appreciable ice thickness along the leading edge. Figure 12 shows several images of the ice formation near the end of run 117. The ice was of generally uniform thickness across the span except near the endwalls. Comparison of the side view (leftmost) and front perspective view (center) images in Figure 12 confirms that more ice accreted near and on the endwall. Just as the ice injection was turned off, a significant portion of the ice formation shed. During ice injection, the images are somewhat obscured due to the flowing ice and water as is evident by comparing the top and bottom sets of images in Figure 12. Just prior to shed, the ice thickness ahead of the leading edge was 1.69±0.15 mm (or ±2 pixels). Increasing the IWC$_i$ to 20 g/m^3 (run 121) produced similar results to14 g/m^3 (run 117). However, the leading-edge ice thickness at the end of run 121 was smaller at 0.69±0.15 mm. The ice thickness measurements were made from lower resolution images from the top-down view which provided 130 pixels of resolution per cm.

There were a couple of general observations of the ice accretions at 93 kPa worth noting. First, it was observed that ice accretion formed both on the titanium and Teflon exposed surfaces. In many cases, more ice accreted near the airfoil ends (both root and tip) than what was seen across the leading edge of the airfoil. Second, the ice was not well adhered to the surface and would often shed either in its entirety or over a portion of the span as seen in Figure 12. This was especially evident just after the run was completed when ice shedding would often occur just a few seconds after the ice flow was turned off.

A good indicator of whether or not ice would form was the surface temperature measurement at the leading edge (thermocouple #1 in Figure 6). Figure 13 shows the leading-edge thermocouple readings for 4 cases at M = 0.2 and a total pressure of 93 kPa. Just prior to initiation of ice flow, the temperature measurements at the leading edge were approximately 1° cooler than the total temperature measurement near the centerline of the tunnel. When the ice flow was turned on, the temperature began to drop almost immediately. In Figure 13, a time of 0 seconds represents a system indication of when the ice flow is turned on. However, there was a lag of few seconds from when the system receives the signal and when ice particles actually start to flow that explains the slight lead in temperature drop seen in the figure. For run 98 which began at ~13.5 °C, the temperature takes almost 30 seconds to reach steady state conditions of approximately 2 °C. For colder initial temperatures of 4 °C (run 115), a steady state of ~1 °C was reached within about 10 seconds with a comparable ice flow. Increasing the ice flow (run 117) reduced the steady-state temperature to about ~0.5 °C. However, a further increase of ice flow to 20 g/m^3 (run 121) did not appreciably change the results from the previous run. Given the observations in Figure 12 and Figure 13, a leading-edge thermocouple reading of about 0.5 °C or less appeared to provide an indication of whether ice would be seen on the surface.

Runs 126 -135 and 158 used a higher Mach number of 0.3. The ice accreted at this higher Mach number generally had a more uniform and solid appearance but a smaller overall shape when compared to those generated at a Mach value of 0.2. Figure 14 shows images from run 132 about a minute after the LWC was increased from 0 to 0.5 g/m^3. With no LWC, there was no ice accreting at this condition. However, ice began to accrete almost immediately after the addition of 0.5 g/m^3 LWC. Some ice accretion is also visible of the suction surface of the airfoil as seen in middle image of Figure 14. At higher LWC values of 3 g/m^3 during run 135, no ice accreted as the surface appeared to be almost all liquid. Once the LWC value was reduced to 2 g/m^3, slushy ice was observed to start accreting during run 135.
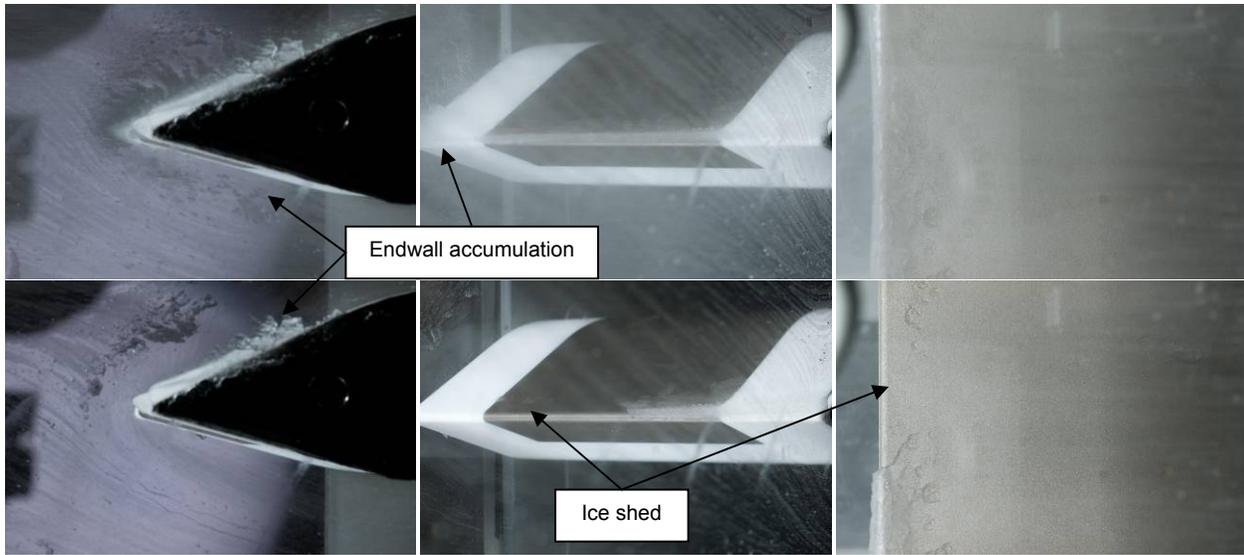
Figure 12.—Images from run 117 just prior to and after injected ice is turned off. A portion of the ice is seen to have shed just in the lower images. The time between the top and bottom images is 5 seconds.
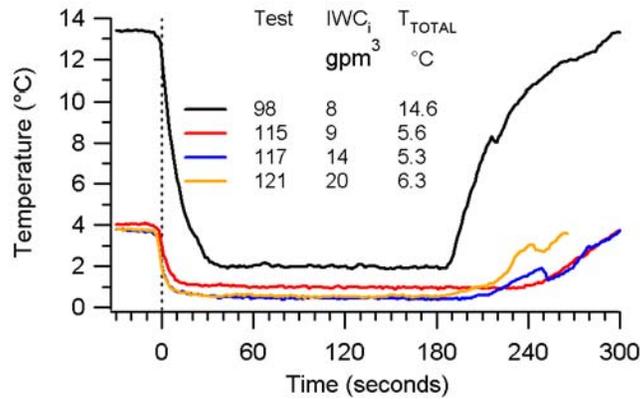
Figure 13.—Leading edge temperature (thermocouple #1) measurements as a function of time during 4 runs at $M = 0.2$ and a total pressure of 93 kPa.

Figure 14.—Images from run 132 about 3 minutes into the test. At this time the LWC value is about 0.5 g/m^3 and was ultimately increased to 1 g/m^3. The ring shape seen in the rightmost image is a reflection of the camera itself from the top window and appears in some of the top-down views.
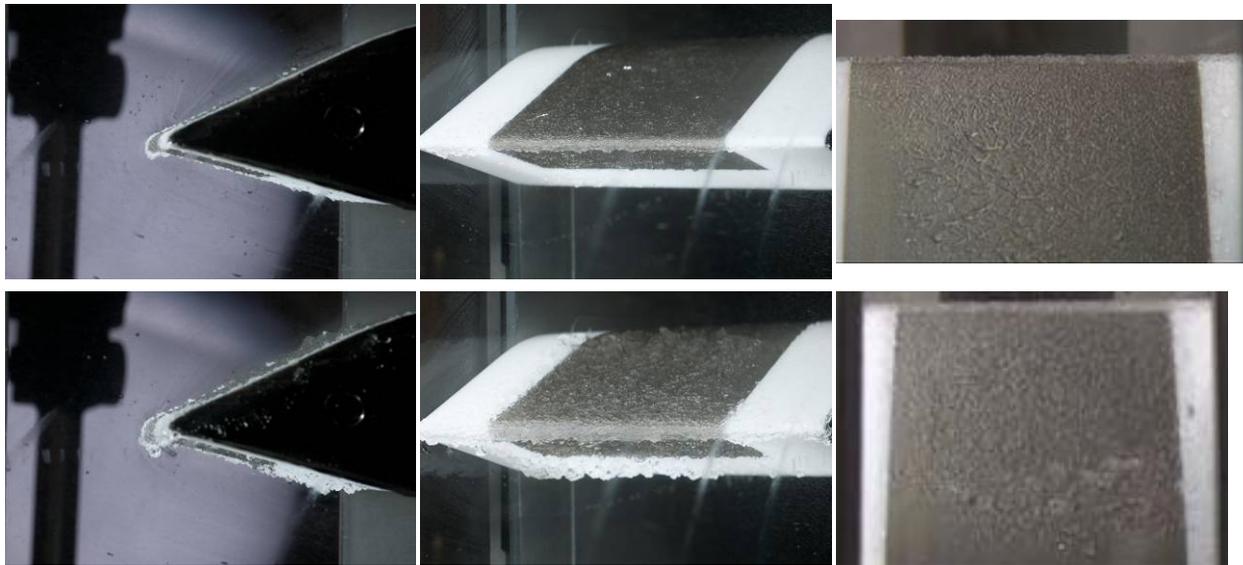
Figure 15.—Images from run 137 (top) and 139 (bottom). The top and bottom images represent about 120 and 200 seconds into the respective runs. During these runs, the top-down still camera view became inadvertently blocked. As such, the top-down images shown are frames from the HD video camera at approximately the same time as the other views. The views from the HD camera are rotated 90° from those of the still camera shown in previous figures with the leading edge of the airfoil at the top of the image.

Starting with run 137, all the remaining runs were conducted at lower pressures, predominately at 45 kPa with just a few runs at 56 kPa due to available test time. A key observation from the lower pressure runs was the ability for glaze-type ice accretions to occur with just LWC being injected (Figure 15). The images in the figure show ice shapes reminiscent of those seen in traditional icing where liquid droplets are supercooled.

Low-pressure runs 141 and 147 were conducted at TAT values of 13.8 and 12.3 °C, respectively, with $IWC_i = 5$ g/m^3 and no injected water, to determine if there was enough natural melt of the ice crystals to allow ice to form on the airfoil. Values of LWC_m were 0.2 and 0.16 g/m^3 for runs 141 and 147, respectively. Small accretions formed at the leading edge in both tests, and a very thin layer of ice formed over the entire flat icing surface in test 147. A similar layer appeared to form in test 141 as well, but it was less noticeable. Runs 144 and 149 were conducted at nominally the same conditions as tests 141 and 147, respectively, but with water added ($LWC_i = 1$ and 2 g/m^3). The additional water produced very large accretions in both cases, with continuous leading-edge growth (Figure 16).

The leading-edge ice growth as a function of time was easily measured from the top-down camera views. The HD video camera data were analyzed as it offered more time resolution compared with the still cameras. Also, for the cases in which the ice growth was substantial such as runs 144 and 149 (which grew out of the field of view for the still cameras), the video camera field of view was adjustable in real time allowing the entire ice growth to be captured. Figure 17 shows the leading-edge ice growth as a function of time for run 149. The measurement was made at mid span using the Spotlight software developed by NASA (Ref. 9). Spotlight can automatically track an intensity value along a given line. In this case, Spotlight began at the top edge of the image, mid-way along the span, and located the brighter pixel corresponding to the edge of the ice. A red cross is shown in the upper right image of Figure 16 which corresponds to the location of the leading-edge ice thickness measurement. Provided there was sufficient contrast between the ice and the background, Spotlight could continue the measurement from frame to frame automatically (for a 180 second run there would be 10,800 frames).
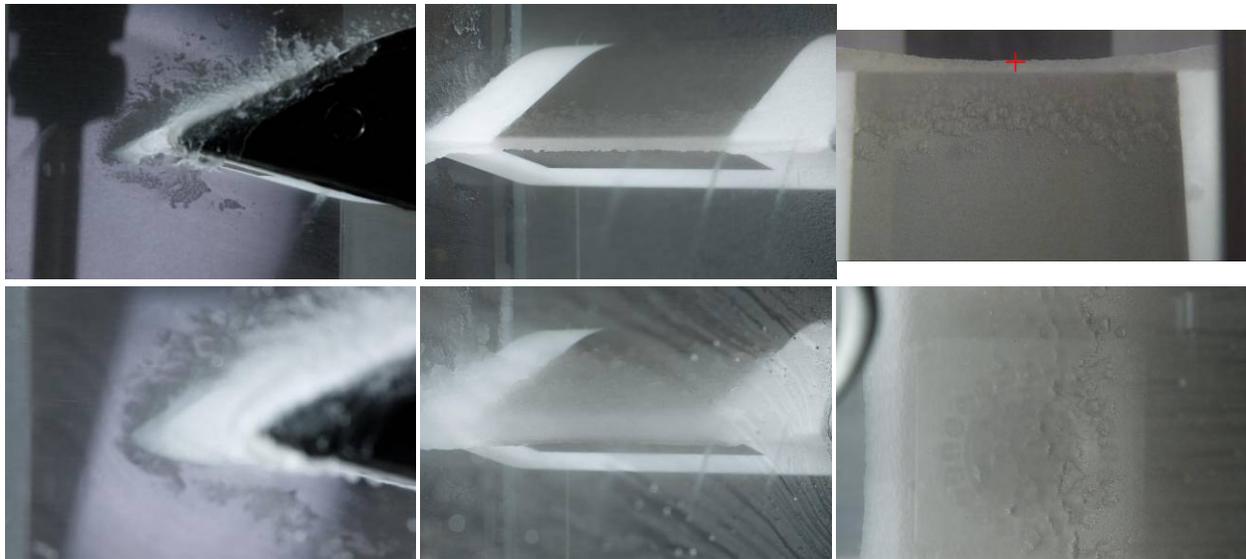
Figure 16.—Images from run 144 (top) and 149 (bottom) showing about 100 seconds into the test. Significant ice accumulations are observed. Similar to Figure 15, the top-down view for run 144 was unavailable and a frame from the video footage was extracted. The leading edge ice as seen from the top-down (rightmost) images eventually grew out of the camera's field of view. The red cross in the upper-right image denotes the location of the leading edge as measured by the NASA Spotlight software.
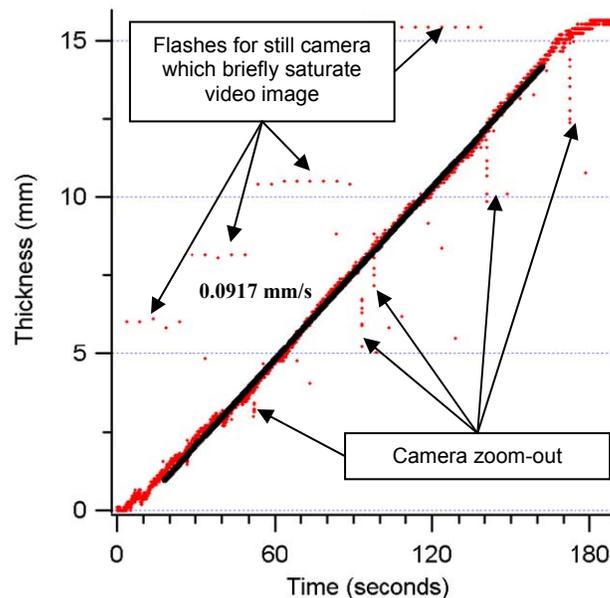
Figure 17.—Ice thickness measurement versus time for run 149. The black line corresponds to a linear curve fit of the data from 10 to 90% of the run duration of 180 seconds.

As seen in Figure 17, the leading-edge growth rate for run 149 was fairly linear with a slope of 0.0917 mm per second, resulting in a thickness over 15 mm in just 3 minutes. Occasionally, anomalies would occur with the automated routine. For example, the flashes for the still cameras would saturate the image thus measuring an artificially high thickness as seen in Figure 17. In addition, the routine needed to be reset each time the camera zoom was changed as this affected the location of mid span on the image and the conversion from pixels to millimeters. An artifact of zoom, which took several frames to reach the new field of view, was the appearance of vertical lines in the thickness vs. time shown in Figure 17.

One final comment about the icing observed at lower pressure was that it generally appeared to be well adhered to the surface. This was especially evident after a given run when the airfoil was to be de-iced in preparation for the subsequent run. Often, it would require significant effort to remove the ice formation including turning off the cold jet flow temporarily to allow the warm to warm the surface. Additionally, the surface heaters (used on the copper insert for the heat transfer measurements, but used on the titanium insert for deicing) were powered to try and loosen the ice. Since the ice would generally remain intact for several minutes after turning on the heaters, even though the insert surface temperatures would climb to over 20 °C, the ice was clearly no longer adhered to the surface but rather was simply anchored to the airfoil by virtue of being wrapped around the blade leading edge as a shell-like structure.

Discussion

As mentioned in the Results section, the ice appeared to be well adhered to the surface in the tests at the lowest pressure (45 kPa), allowing it to develop over a large portion of the forebody pressure surface in all cases where accretion was observed. Such widespread deposits were never observed in the tests at the highest pressure, where the accretions were usually limited to a small area around the leading-edge stagnation line, which was roughly at the top of the leading-edge semi ellipse at –6° angle-of-attack. The bottom (suction surface) half of the leading-edge semi ellipse, where surface velocities exceed freestream values by almost 70% (corresponding to a minimum Cp of –1.9, as seen in Figure 10 and Figure 11) with a clean surface, was typically ice-free in the tests at high pressure, but not at low pressure. The larger accretions observed at low pressure were generally accompanied by lower surface temperatures.
The icing behavior at low and high pressure appeared to be correlated with the wet-bulb temperature (T_{wb}), which was above freezing in all of the tests at 93 kPa and below freezing in all of the tests at lower pressure. Ice accretion over the entire forebody pressure surface was observed in tests 137 and 139 at 45 kPa, where only liquid water was injected and estimated T_{WB} values based on freestream and total conditions ($T_{WB\infty}$ and T_{WBo}, respectively) were in the range $-2.7 \rightarrow -4$ °C. Since T_{WB} is defined as the temperature of an adiabatic wet surface in air, freezing of water on such a surface can be expected for a local $T_{WB} < 0$ °C, where the local value should strictly be calculated with the local static pressure and recovery temperature. Freezing would be expected everywhere on the blade surface when $T_{WBo} < 0$ °C, however, since this is the highest possible value on the blade surface.

Although the titanium surface of the wedge airfoil is not strictly adiabatic, T_{WB} is probably still useful for obtaining a first order estimate of the wet surface temperature because the back surface of the 3.18 mm thick surface is effectively adiabatic and Ti 6Al-4V has a very low thermal conductivity, only ~7 W/m K. A more precise estimate of the temperature of the wet blade surface temperature could be obtained by accounting for all of the energy (and mass) fluxes to and from the blade surface, including conduction within the blade wall and the flux resulting from a difference between impinging droplet temperature and T_{WB} (these temperatures are assumed equal when calculating T_{WB}). Icing simulation codes such as GlennICE (Ref. 10) are capable of performing such calculations.

Reduced air pressure increases evaporation and thereby reduces T_{WB}, so the potential for evaporation-enhanced freezing at a fixed dry bulb temperature and moisture content (specific humidity) increases as air pressure decreases. For example, with the specific humidity which applied in test 149, 0.00155 kg H_2O vapor/kg dry air, a dry bulb temperature < 6.5 °C is required to obtain $T_{WB}<0$ °C at sea level (101 kPa), whereas a dry bulb temperature < 21 °C will give $T_{WB}<0$ °C at 45 kPa.

The large (adhered) ice accretions that were observed in the low pressure tests would undoubtedly cause the aerodynamic performance of a compressor stator or guide vane to degrade significantly, and could significantly damage downstream components if and when they shed from the blade. These effects would not be nearly as severe with the small accretions observed in the high pressure tests, so the authors believe that it is important to get a better understanding of the conditions under which accretions of the first variety can occur, and in particular the role of wet-bulb temperature or, more generally, evaporative cooling. Future tests and analyses will address these issues. Other geometries and conditions which might be more conducive to obtaining large accretions of loosely or non-adhered ice, such as those involving

lower Mach numbers and geometries which can more effectively trap ice, such as blade-endwall junctions, will also be investigated.

Summary

The aviation industry has experienced numerous engine power loss events associated with high-altitude convective weather and often in a warm tropical environment. Hypotheses for ice accretion due to ice-crystal ingestion within an engine are starting to be investigated. NASA and NRC, with sponsorship by the Federal Aviation Administration and Transport Canada, are beginning a series of experiments to examine the physical mechanisms of ice accretion on surfaces exposed to ice-crystal and mixed-phase conditions similar to those encountered during engine power-loss events. In November 2010, two weeks of testing occurred at the NRC RATFac facility capable of providing ice-crystal and mixed-phase conditions with altitude variation.

The tests utilized a single wedge-type airfoil which was designed to facilitate fundamental studies while still retaining critical features of a compressor stator blade or guide vane. The airfoil's test surface was made of copper or titanium in an otherwise Teflon airfoil. The copper airfoil was instrumented with thermocouples and heat-flux gauges while the titanium with only thermocouples. The airfoil was placed at angle of attack in the NRC cascade wind tunnel which consisted of an inlet duct with a bell mouth rectangular inlet and test section. Both aerodynamic (sans ice and water injection) as well as icing tests were performed. For a portion of the aerodynamic tests, the center section of the airfoil was replaced with a hollow aluminum insert with taps for the purpose of measuring the static pressure distribution. Still and video cameras captured high resolution images of three views of the test article. The imaging data were used for both observations and quantitative measurements.

For the aerodynamic tests, conditions included angles of attack of 0° and –6° at Mach 0.2, 0.3, and 0.4, and nominal stagnation pressures of 45 and 93 kPa. The corresponding chord Reynolds number ranged from approximately 0.45×10^6 to 1.8×10^6. The total air temperature ranged from approximately 8 to 20 °C. Results from the aerodynamic testing showed excellent agreement between the experimental and CFD data on the pressure surface upstream of $x/c = 0.25$ which was the icing-test surface of interest. In general, flow over the icing surface on the pressure side was well-behaved for the ice-accretion studies over the desired range of conditions. Several runs were repeated, demonstrating good repeatability in the data.

During the aerodynamic testing, the copper covered airfoil was used to measure heat-transfer coefficients at tunnel Mach numbers of 0.215, 0.25, and 0.32; and a total temperature and total pressure of ~10 °C and 45 kPa, respectively. The heat-transfer coefficients were calculated from the measured heat fluxes and temperature differences between the surface and recovery temperatures at various locations along the airfoil with some corrections to account for the presence of the gauge itself. The calculated heat transfer coefficient values ranged from about 110 to 180 W/m^2K.

Icing tests were performed for flow speeds ranging from M = 0.2 to 0.3 at total pressures from 93 to 45 kPa and total temperatures from 5 to 15 °C. Ice- and liquid-water contents ranged up to 20 and 3 g/m^3, respectively. The ice accretions at M = 0.3 generally had a more uniform and solid appearance but a smaller overall shape when compared to those generated at M = 0.2. The ice appeared to be well adhered to the surface in the tests at the lowest pressure (45 kPa), allowing it to develop over most of the forebody pressure surface in all cases where accretion was observed. In several cases, continuous leading-edge ice growth was observed. For a particular case, measurements from video data showed a thickness in excess of 15 mm over a period of just 3 minutes. Such widespread deposits were never observed in the tests at the highest pressure, where the accretions never covered the entire test surface and were usually limited to a small area around the leading edge. The bottom (suction) surface was typically ice-free in the tests at high pressure, but not at low pressure. The larger accretions observed at low pressure were generally accompanied by lower surface temperatures. A good indicator of whether or not ice would form was a surface temperature measurement near 0 °C at the leading edge.

The icing behavior at low and high pressure appeared to be correlated with the wet-bulb temperature (T_{wb}), which was above freezing in all of the tests at 93 kPa and below freezing in all of the tests at lower pressure. Since T_{WB} is defined as the temperature of an adiabatic wet surface in air, freezing of water on such a surface can be expected for a local $T_{WB} < 0$ °C. Reduced air pressure increases evaporation and thereby reduces T_{WB}, so the potential for evaporation-enhanced freezing at a fixed dry bulb temperature and moisture content (specific humidity) increases as air pressure decreases. The large (adhered) ice accretions that were observed in the low-pressure tests would undoubtedly cause the aerodynamic performance of a compressor stator or guide vane to degrade significantly, and could significantly damage downstream components if shed from the blade. The authors believe that it is important to get a better understanding of the conditions under which accretions of the first variety can occur, and in particular the role of wet-bulb temperature or, more generally, evaporative cooling.

Future Work

Two additional weeks of testing were just completed (March 2011) at the time of this paper's completion. During these tests, a new humidity-control system was used for the first time which allowed independent control of the humidity in the airstream of the test section. Additionally, the moisture content of the test-section air could also be independently measured. Among various objectives, one new aspect of the March testing focused on better understanding of how humidity affects the icing process in ice-crystal and mixed-phase conditions. Specifically, the wet-bulb temperature was investigated as a primary parameter which could indicate the onset of icing. Results from the March 2011 tests are currently under analysis and will be reported in a subsequent paper. Testing beyond the March 2011 test weeks is currently anticipated pending funding availability. Finally, NASA plans to use the data from this testing to further develop the icing code GlennICE (Ref. 10) for simulating the ice accretion.

Appendix

TABLE A1.—SYMMETRICAL AIRFOIL UPPER
SURFACE COORDINATES AND Ti INSERT
INNER SURFACE COORDINATES

Airfoil Upper Surface			Ti Insert Inner Surface		
Point	X (mm)	Y (mm)	Point	X (mm)	Y (mm)
1	0.00	0.000	24	84.67	24.31
2	0.03	0.27	25	76.62	17.20
3	0.11	0.53	26	75.39	18.59
4	0.25	0.77	27	78.60	21.43
5	0.43	0.98	28	71.49	21.07
6	0.77	1.25	29	64.44	20.10
7	1.13	1.500	30	57.49	18.54
8	1.52	1.71	31	50.70	16.39
9	1.92	1.88	32	10.06	1.60
10	49.66	19.25	33	9.55	1.30
11	55.04	21.01	34	9.17	0.85
12	60.53	22.42	35	8.97	0.30
13	66.10	23.46	36	8.94	0.00
14	71.73	24.14	37	8.97	−0.30
15	77.39	24.45	38	9.17	−0.85
16	83.06	24.39	39	9.55	−1.30
17	88.71	23.96	40	10.06	−1.60
18	94.32	23.16	41	25.24	−7.12
19	220.09	0.98	42	23.34	−3.05
20	220.42	0.86	43	25.02	−2.27
21	220.68	0.64	44	29.53	−11.93
22	220.86	0.34			
23	220.92	0.000			

Notes:
   Segments with endpoints 9, 10 and 18, 19 are straight lines.
   Segments with points 10-18 define an 86.6 mm radius 30° arc.
   All Ti insert inner surface (non-wetted) segments except those
      with endpoints 27-31 and 32-40 are straight lines.

References

1. Mason, J. G., Strapp, J. W., and Chow, P. "The Ice Particle Threat to Engines in Flight," *44th AIAA Aerospace Sciences Meeting and Exhibit*, AIAA-2006-206, 2006.
2. MacLeod, J. "Development of Ice Crystal Facilities for Engine Testing," *2007 SAE Aircraft and Engine Icing International Conference*, 2007-01-3290, 2007.
3. Mason, J. G., Chow, P., and Fuleki, D. M. "Understanding Ice Crystal Accretion and Shedding Phenomenon in Jet Engines using a Rig Test," *ASME Turbo Expo 2010*, GT2010-22550, 2010.
4. Fuleki, D. M., and MacLeod, J. D. "Ice Crystal Accretion Test Rig Development For A Compressor Transition Duct," *AIAA Guidance, Navigation, and Control Conference*, AIAA 2010-7529, 2010.
5. Knezevici, D. C., Fuleki, D., and MacLeod, J. "Development and Commissioning of the Linear Compressor Cascade Rig for Ice Crystal Research," *International Conference on Aircraft and Engine Icing and Ground Deicing*, 2011-38-0079, 2011.
6. Barlow, J. B., Rae, W. H. J., and Pope, A. *Low-Speed Wind Tunnel Testing*. New York, NY: John Wiley & Sons, 1999.
7. Allen, H. J., and Vincenti, W. G. "Wall Interference in a Two-Dimensional-Flow Wind Tunnel with Consideration of the Effect of Compressibility," No. NACA TR-782, 1944.
8. Drela, M., and Youngren, H. "XFOIL 6.94 User Guide," 2001.
9. Klimek, R., and Wright, T. "Spotlight: Image Analysis and Object Tracking Software." 2005.11.12 ed., NASA Glenn Research Center, Cleveland, OH, 2005.
10. Wright, W. B., Jorgenson, P. C. E., and Veres, J. P. "Mixed Phase Modeling in GlennICE with Application to Engine Icing," *AIAA Atmospheric and Space Environments Conference*, AIAA 2010-7674, 2010.

REPORT DOCUMENTATION PAGE		Form Approved OMB No. 0704-0188

The public reporting burden for this collection of information is estimated to average 1 hour per response, including the time for reviewing instructions, searching existing data sources, gathering and maintaining the data needed, and completing and reviewing the collection of information. Send comments regarding this burden estimate or any other aspect of this collection of information, including suggestions for reducing this burden, to Department of Defense, Washington Headquarters Services, Directorate for Information Operations and Reports (0704-0188), 1215 Jefferson Davis Highway, Suite 1204, Arlington, VA 22202-4302. Respondents should be aware that notwithstanding any other provision of law, no person shall be subject to any penalty for failing to comply with a collection of information if it does not display a currently valid OMB control number.
PLEASE DO NOT RETURN YOUR FORM TO THE ABOVE ADDRESS.

1. REPORT DATE (DD-MM-YYYY) 01-05-2012	2. REPORT TYPE Technical Memorandum	3. DATES COVERED (From - To)
4. TITLE AND SUBTITLE Fundamental Ice Crystal Accretion Physics Studies		**5a. CONTRACT NUMBER**
		5b. GRANT NUMBER
		5c. PROGRAM ELEMENT NUMBER
6. AUTHOR(S) Struk, Peter, M.; Broeren, Andy, P.; Tsao, Jen-Ching; Vargas, Mario; Wright, William, B.; Currie, Tom; Knezevici, Danny; Fuleki, Dan		**5d. PROJECT NUMBER**
		5e. TASK NUMBER
		5f. WORK UNIT NUMBER WBS 648987.02.02.03.10
7. PERFORMING ORGANIZATION NAME(S) AND ADDRESS(ES) National Aeronautics and Space Administration John H. Glenn Research Center at Lewis Field Cleveland, Ohio 44135-3191		**8. PERFORMING ORGANIZATION REPORT NUMBER** E-18119
9. SPONSORING/MONITORING AGENCY NAME(S) AND ADDRESS(ES) National Aeronautics and Space Administration Washington, DC 20546-0001		**10. SPONSORING/MONITOR'S ACRONYM(S)** NASA
		11. SPONSORING/MONITORING REPORT NUMBER NASA/TM-2012-217429
12. DISTRIBUTION/AVAILABILITY STATEMENT Unclassified-Unlimited Subject Category: 03 Available electronically at http://www.sti.nasa.gov This publication is available from the NASA Center for AeroSpace Information, 443-757-5802		
13. SUPPLEMENTARY NOTES		

14. ABSTRACT
Due to numerous engine power-loss events associated with high-altitude convective weather, ice accretion within an engine due to ice-crystal ingestion is being investigated. The National Aeronautics and Space Administration (NASA) and the National Research Council (NRC) of Canada are starting to examine the physical mechanisms of ice accretion on surfaces exposed to ice-crystal and mixed-phase conditions. In November 2010, two weeks of testing occurred at the NRC Research Altitude Facility utilizing a single wedge-type airfoil designed to facilitate fundamental studies while retaining critical features of a compressor stator blade or guide vane. The airfoil was placed in the NRC cascade wind tunnel for both aerodynamic and icing tests. Aerodynamic testing showed excellent agreement compared with CFD data on the icing pressure surface and allowed calculation of heat transfer coefficients at various airfoil locations. Icing tests were performed at Mach numbers of 0.2 to 0.3, total pressures from 93 to 45 kPa, and total temperatures from 5 to 15 °C. Ice and liquid water contents ranged up to 20 and 3 g/m^3, respectively. The ice appeared well adhered to the surface in the lowest pressure tests (45 kPa) and, in a particular case, showed continuous leading-edge ice growth to a thickness greater than 15 mm in 3 min. Such widespread deposits were not observed in the highest pressure tests, where the accretions were limited to a small area around the leading edge. The suction surface was typically ice-free in the tests at high pressure, but not at low pressure. The icing behavior at high and low pressure appeared to be correlated with the wet-bulb temperature, which was estimated to be above 0 °C in tests at 93 kPa and below 0 °C in tests at lower pressure, the latter enhanced by more evaporative cooling of water. The authors believe that the large ice accretions observed in the low pressure tests would undoubtedly cause the aerodynamic performance of a compressor component such as a stator blade to degrade significantly, and could damage downstream components if shed.

15. SUBJECT TERMS Icing; Engine icing				

16. SECURITY CLASSIFICATION OF:			17. LIMITATION OF ABSTRACT	18. NUMBER OF PAGES	19a. NAME OF RESPONSIBLE PERSON STI Help Desk (email:help@sti.nasa.gov)
a. REPORT U	b. ABSTRACT U	c. THIS PAGE U	UU	33	19b. TELEPHONE NUMBER (include area code) 443-757-5802

Standard Form 298 (Rev. 8-98)
Prescribed by ANSI Std. Z39-18